JGR: Solid Earth

Supporting Information for

The Frictional-Viscous Transition in Experimentally Deformed Granitoid Fault Gouge

Weijia Zhan[1], André R. Niemeijer[2], Alfons Berger[1], Natalia Nevskaya[1], Christopher J. Spiers[2], Marco Herwegh[1]

[1]Institute of Geological Sciences, University of Bern, Bern, Switzerland.

[2]High Pressure and Temperature Laboratory, Utrecht University, Utrecht, the Netherlands.

Contents of this file

Text S1.

All XRD powder patterns were measured with a PANalytical Empyrean diffractometer equipped with a Cu X-ray source (45kV/ 40mA). In the whole rock analysis, corundum powder (Al_2O_3) of known amount was added to the bulk sample as the internal standard (Dinnebier and Billinge, 2008). Rietveld refinement method in TOPAS® software was used to determine the weight percentage of identified phases (Rietveld, 1969). The particle size distribution of simulated gouge powders was determined using a Malvern Mastersizer 2000 laser diffractometer at Geographisches Institut at University of Bern, Switzerland.

Text S2.

Image processing and analysis is subdivided into three steps: pixel classification, object classification and quantitative analysis (Figure S1). An interactive machine-learning tool named ilastik (https://www.ilastik.org/; Berg et al., 2019) was used for pixel classification and object classification, while ImageJ (https://imagej.nih.gov/ij/) was used for quantitative analysis. In the first step, a sufficient number of pixels of the original BSE images (Figure S2 A) were manually labelled as either 'particles' or 'openings' until the algorithm achieved a reliable estimation of the remaining pixels. This classification produced probability maps (Figure S2 B) indicating the likelihood of each pixel to belong in specific class. Pixels with a probability $\geqslant$ 0.8 were designated as 'particles', while the rest were classified as 'openings'. In the second step, the probability maps of were used as the input data for object classification. 'Openings' were further categorized into 'pores' and 'cracks' based on their object-level features. 'Pores' are isolated openings, while 'cracks' are interconnected openings. Finally, object prediction maps were imported into ImageJ for segmentation and quantitative analysis. Only particles larger than 1 μm^2 (~120 $pixel^2$) were classified as 'clasts'. We assume that 'matrix' covers the remaining area after subtracting the total area of clasts, pores and cracks from the entire image area. This is because matrix consists of extremely small particles that are difficult to manually label and threshold.

Microstructures of sample u1038 quantitatively analyzed using the workflow described above in order to determine the size of the representative element volumes, thereby defining the minimum area size necessary for an optimally precise analysis (Akker et al., 2018; Kanit et al., 2003) (Figure S2 C). We plotted the mean clast diameters ($\bar{d}_i, \mu m$) and mode clast diameters ($d_{i\_m}, \mu m$) against the length of analyzed area. As demonstrated in Figure S2 D, the mean and mode clast diameters achieved a consistent state once the analyzed area exceeded a length of 120 μm, indicating that the representative element volumes are 120 μm in length.

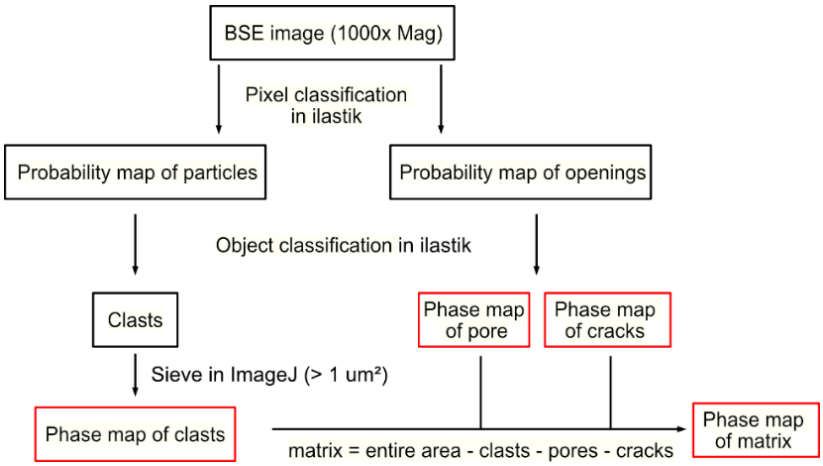

Figure S1. Workflow of image analysis using backscatter images.

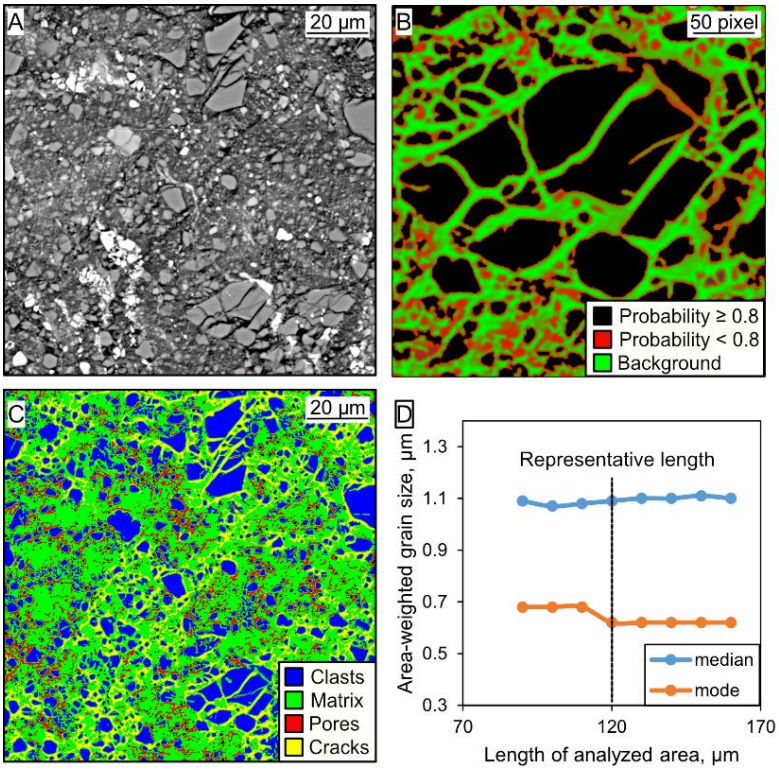

Figure S2. Schematic procedure of image analysis (taking u1038 as an example). (A) original BSE image with 1000x magnification; (B) Probability map after pixel classification; (C) Object prediction map after object classification; (D) Effect of the size of analyzed area and the area-weighted grain size distribution.

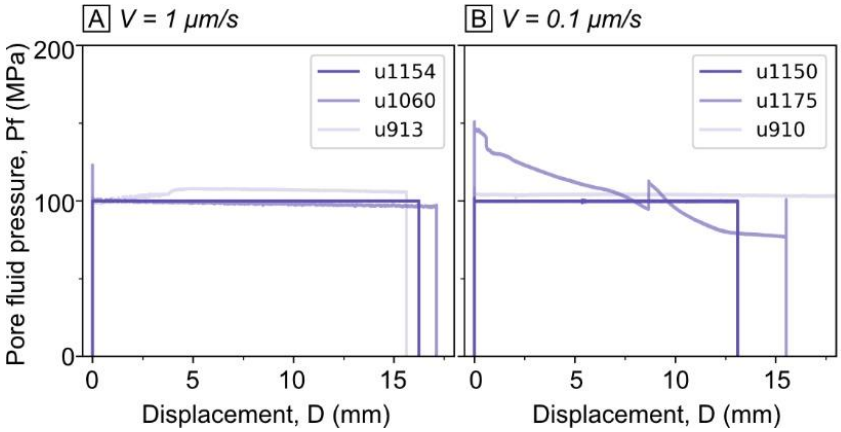

Figure S3. Plot of pore fluid pressure against shear displacement for experiments (A) at V = 1 µm/s and (B) V = 0.1 µm/s. The fluctuations in pore fluid pressure under constant normal stress affect the seal friction and, therefore, the shear stress.

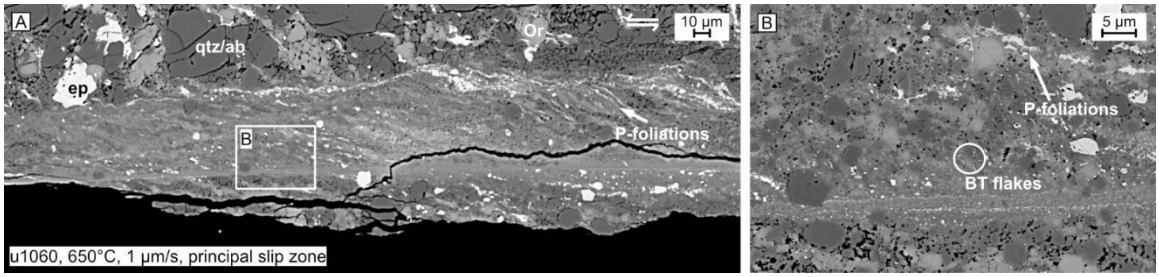

Figure S4. Mosaics of backscatter images of the principal slip zone of experiments u1060, showing the well-developed P-foliations defined by aligned biotite. The white box indicates the location of the close-up, shown in (B).

Experiments	Temperature (°C)	Thickness of whole gouge layer (μm)	Slip zone				Principal slip zone			
			W (μm)	N	$\bar{d}_m$ (μm)	$\bar{d}$ (μm)	W (μm)	N	$\bar{d}_m$ (μm)	$\bar{d}$ (μm)
$V = 100\ \mu m/s$										
u1051	20	758	174	143	1	6	-	-	-	-
u1049	200	726	175	175	2	3	-	-	-	-
u1052	450	803	181	159	2	4	-	-	-	-
u1059*	650	461	176	12	2	3	-	-	-	-
$V = 1\ \mu m/s$										
u1038	20	500	195	1150	2	4	-	-	-	-
u908	200	450	149	789	1	5	-	-	-	-
u909	450	809	333	25	1	2	83	89	0.2	0.6
u1154	650	715	238	53	2	2	83	45	0.5	0.7
u913*	650	893	184	1845	2	7	42	58	0.6	1.2
u1060*	650	486	73	1988	2	7	40	191	0.4	1.7
$V = 0.1\ \mu m/s$										
u1157	20	658	198	249	1	3	-	-	-	-
u1153	200	791	192	1247	3	7	120	837	0.2	0.5
u1151	450	658	235	52	2	4	17	544	0.3	1.2
u1150	650	485	141	13	1	2	31	21	0.4	0.6
u910*	650	727	208	59	2	3	20	143	0.5	1.1

Table S1. List of the width, median, and mean particle size of the slip zone and principal slip zone (PSZ) of all experiments conducted in this study, except for u1175 (no thin section). The particle size calculation includes only clasts for the slip zone, but covers both clasts and matrix for the PSZ. Note that the particle size presented in this table is only semi-quantitative due to the limited count number. N = count numbers, W = width measured from the collected sample, $\bar{d}_m$ = median diameter, $\bar{d}$ = mean diameter.

Reference	Material	T (°C)	σ_n^{eff} (MPa)	P_f (MPa)	V (μm/s)	μ_{ss} (-)
Granitoid materials						
Lockner et al., 1986	granite gouge	22-845	250 (confining pressure)	dry	0.055-5.5	0.69-0.77
Mitchell et al., 2016	westerly granite gouge	20-600	5	dry	0.3-30	0.68-0.82
Blanpied et al., 1995	westerly granite gouge	23-600	400	100	0.001-1	0.53-0.74
An et al., 2021	granodiorite gouge	100-200	110	42	0.0488-1.22	0.70-0.72
Lei et al., 2022a	natural granitic gouge	25-600	200	30	0.04-1	0.67-0.71
Other materials						
Niemeijer et al., 2008	quartz gouge	400-600	20	200	1	0.54-0.71
Okuda et al., 2023	basaltic gouge (~50% albite, ~27% clinopyroxene, ~15% chlorite, ~8% opaque minerals)	100-550	100	100	1-100	0.45-0.7
den Hartog et al., 2013	100% muscovite	200-600	170	100	1-100	0.45-0.65
Lu & He, 2014	100% biotite	25-600	120-200	10-100	0.122-1.22	0.25-0.44

Table S2. List of experimental conditions from previous studies (An et al., 2022; Blanpied et al., 1995; Lei et al., 2022; Lockner & Byerlee, 1986; Mitchell et al., 2016; Okuda et al., 2023). T: temperature, σ_n^{eff}: effective normal stress, P_f: pore fluid pressure, V: sliding velocity, μ_{ss}: apparent friction coefficient at (near) steady-state condition.

Experiments	Velocity (μm/s)	Localized domain	Width of localized domain, W (μm)	Shear strain rate, $\dot{\gamma}$ (s^{-1})	(Equivalent) Strain rate, $\dot{\varepsilon}$ (s^{-1})	Shear stress, τ_{ss} (MPa)	(Equivalent) Differential stress, σ (MPa)	Stress sensitivity exponent n
T = 20°C								
u1051	100	Slip zone	174	0.575	0.160	74.50	129.04	
u1038	1	Slip zone	195	0.005	0.003	81.11	140.49	~17
u1157	0.1	Slip zone	198	0.001	0.0002	65.82	114.04	
T = 200°C								
u1049	100	Slip zone	175	0.571	0.275	73.58	127.44	-
u908	1	Slip zone	149	0.007	0.004	75.41	130.61	
T = 450°C								
u1052	100	Slip zone	181	0.552	0.319	77.40	134.06	-
T = 650°C								
u1154	1	PSZ	83	0.012	0.007	67.83	117.49	
u913	1	PSZ	42	0.024	0.014	49.78	86.22	
u1060	1	PSZ	40	0.025	0.014	63.94	110.75	~2
u1150	0.1	PSZ	31	0.003	0.002	49.70	86.08	
u910	0.1	PSZ	20	0.005	0.003	37.27	64.55	

Table S3. List of data plotted in Figure 9 to obtain the stress sensitivity exponent *n*.